Microwave and submillimeter spectroscopy of Ar–NH_3 states correlating with Ar + NH_3 ($j=1,|k|=1$)

E. Zwart, H. Linnartz, and W. Leo Meerts
Fysisch Laboratorium, University of Nijmegen, Toernooiveld, 6525 ED Nijmegen, The Netherlands

G. T. Fraser
Molecular Physics Division, National Institute of Standards and Technology, Gaithersburg, Maryland 20899

D. D. Nelson, Jr.[a] and W. Klemperer
Department of Chemistry, Harvard University, Cambridge, Massachusetts 02138

(Received 24 December 1990; accepted 25 March 1991)

Microwave and submillimeter transitions for Ar–NH_3 have been observed and assigned for the Σ and Π states correlating asymptotically with Ar + NH_3 ($j=1,|k|=1$). The Σ states are found to lie below the Π states and are separated by approximately the inversion splitting of free NH_3. For the Π states the NH_3 inversion tunneling is nearly quenched, being only weakly allowed through Coriolis interactions with the nearby Σ states. The observed microwave and submillimeter spectra also allow the determination of ^{14}N quadrupole coupling constants and relative submillimeter absorption intensities. All the above results are interpreted using a model internal–rotation inversion Hamiltonian, leading to detailed information about the anisotropy of the intermolecular potential.

I. INTRODUCTION

The investigation of weakly bound complexes involving NH_3 allows the systematic examination of the effects of the van der Waals interaction on the NH_3 inversion tunneling. In free NH_3 this tunneling motion has been well studied using microwave and infrared spectroscopy. The tunneling splitting for the ground vibrational state is found to be 0.8 cm^{-1}, increasing to 36 cm^{-1} for the first excited vibrational state (ν_2) associated with the umbrella coordinate.[1]

Upon complexation NH_3 generally acts as a hydrogen acceptor and binds axially or near axially to its binding partner.[2] This leads to a large asymmetry in the NH_3 inversion potential which quenches the tunneling. Ar–NH_3 has been regarded as an exception to this case. Using molecular-beam electric-resonance spectroscopy (MBER) Fraser *et al.*[3] reported, without rotational assignment, a series of transitions for Ar–NH_3 between 19 and 20 GHz which they interpreted as direct inversion transitions. Fraser *et al.*[3] also observed an infrared transition from the ground vibrational state of the complex to the ν_2 excited state. Bizarri *et al.*[4] later found two more such transitions, located 32 and 36 cm^{-1} above the transition of Fraser *et al.*[3] Since the inversion splitting of the ν_2 excited state of free NH_3 is 36 cm^{-1}, these infrared observations were taken as further evidence that the NH_3 inversion frequency is essentially unchanged upon complexation.

In a more recent microwave study, Nelson *et al.*[5] observed an additional set of transitions for Ar–NH_3 which they assigned to the ground state of the complex, correlating asymptotically with Ar + NH_3 ($j=0,k=0$). Here, j and k are the rotational quantum numbers for free NH_3. The measured electric dipole moment and nuclear quadrupole coupling constant indicate that the NH_3 subunit is undergoing nearly free internal rotation within the complex. Further evidence for the free-rotor picture came from several far-infrared[6–8] and mid-infrared[9,10] investigations of other Ar–NH_3 states correlating with NH_3 ($j,k=0$). In addition, two different *ab initio* calculations of the potential energy surface have recently been performed by Chalasiński *et al.*[11] and by Bulski *et al.*,[12] respectively. The latter calculations were combined with dynamical modeling[13,14] to provide additional insight into the internal-rotation dynamics of this complex.

The nearly free internal rotation of the NH_3 unit within the complex allows us to describe the internal rotor states of Ar–NH_3 by their correlation with Ar + NH_3 (j,k). There exist two distinct nuclear-spin modifications of Ar–NH_3 which are denoted by ortho and para. Collision-induced or electric-multipole transitions between these two spin states are "nuclear-spin" forbidden. The lowest energy ortho state correlates with Ar + NH_3 ($j=0,k=0$); the lowest energy para state with Ar + NH_3 ($j=1,|k|=1$). The effect of NH_3 inversion tunneling is similar to that in free NH_3. Every j,k state of Ar–NH_3 is tunneling doubled. For the $k=0$ ortho state one of these components has a statistical weight of zero. This makes it difficult to get direct information on the NH_3 inversion splitting in these states. For para Ar–NH_3 both components of the inversion doublet have a nonzero statistical weight.

In the present paper we present microwave and submillimeter measurements of these para states and interpret the results using a model internal–rotation inversion Hamiltonian. For Ar–NH_3 ($j=1,|k|=1$) two types of internal-rotor states result, denoted $\Pi(j=1,|k|=1)$ and $\Sigma(j=1,|k|=1)$, corresponding to whether the internal an-

[a] Present address: Aerodyne Research Corporation, 45 Manning Road, Billerica, MA 01821.

gular momentum is directed along (Π) or perpendicular to (Σ) the radial coordinate. We find for the Σ states that the inversion tunneling splitting is nearly the same as in free NH_3, whereas for the Π states the resulting asymmetry of the NH_3 inversion potential nearly quenches tunneling. Only by Coriolis mixing of the Π and Σ states via overall rotation is tunneling allowed for the Π state. This same Coriolis interaction is the source of the intensity for the pure-inversion Q branch initially observed by Fraser *et al.*[3] near 19.5 GHz.

II. EXPERIMENT

The molecular-beam measurements were done using microwave spectrometers at NIST and Harvard University and a submillimeter spectrometer at the University of Nijmegen. In each case, a molecular beam of Ar–NH_3 was produced by an adiabatic expansion of an NH_3/Ar or an NH_3/Ar/He mixture. The cold rotational temperatures produced by the expansions (1–10 K), together with the large rotational constant of NH_3 ensures that most of the Ar–NH_3 molecules will be in the lowest levels correlating with Ar–NH_3 ($j=0,k=0$) (ortho) or Ar–NH_3 ($j=1,|k|=1$) (para).

The microwave results consist of previously unassigned molecular-beam electric-resonance transitions[3] and new pulsed-nozzle Fourier-transform microwave (FTMW) and electric-resonance optothermal (EROS) measurements. The FTMW[15,16] and EROS[17,18] apparatus have been described in detail elsewhere.

The submillimeter apparatus is based on the direct absorption of harmonics from a klystron by a planar supersonic jet.[19] The harmonics are generated in a Schottky barrier diode and are radiated into free space by a 2 mm long antenna backed by a movable corner reflector. Klystrons around 60 or 70 GHz were used in most cases. A parabolic mirror located approximately 10 cm from the antenna produces a parallel beam of radiation. The desired harmonic is selected using a monochromator with a grating of 0.8 or 1.3 grooves/mm. The radiation is guided by lenses and mirrors through the supersonic jet onto an InSb hot-electron bolometer. The radiation is frequency modulated at 5 kHz and the detector output is monitored at twice this frequency using a phase-sensitive detector. The planar jet is produced by expanding a mixture of a few per cent NH_3 in Ar through a 4 cm long $\times$ 15 μm wide slit nozzle[20] at a backing pressure of approximately 600 Torr.

Approximate relative integrated absorption intensities of the submillimeter transitions were determined by normalizing the observed signal by the total power, measured immediately after recording a transition. To obtain integrated absorption intensities, both the height and the width of a line have to be determined. The recorded line shapes are determined by several factors, including Doppler and pressure broadening, unresolved quadrupole hyperfine structure and the frequency modulation (FM) amplitude. The product of the height and the width of a line can be estimated by determining the peak height as a function of the FM amplitude. This product of height and width is used to determine relative integrated absorption intensities. This procedure has proven useful here, since we are only interested in relative intensities. The estimated uncertainties in the measured relative intensities are 30%. The accuracy is sufficient to determine several striking intensity effects, as will be discussed later.

III. RESULTS

In Sec. IV below a dynamical model is presented to interpret the observed spectrum. Here, we will give a qualitative picture of the dynamics to clarify the spectral observations. The energy-level scheme can be understood by taking an approach similar to that used to discuss Ar–H_2O.[21–23] Here, we have the additional complication of the NH_3 inversion. The states of Ar–NH_3 are described by a model in which the inversion and free rotation of the NH_3 subunit are hindered by the anisotropy of the interaction with the Ar atom. The observed states correlate asymptotically with Ar + NH_3 ($j=1,|k|=1;v=0,1$), where $v=0$ and 1 denote the symmetric and antisymmetric tunneling states, respectively. In the left-hand side of Fig. 1 the energy level diagram for Ar–NH_3 is shown at infinite radial separation, where the potential interaction between the Ar and NH_3 vanishes.

In the right-hand side of Fig. 1, the energy-level scheme which results from the anisotropic interaction of the NH_3 with the Ar is given. Ignoring tunneling, van Bladel *et al.*[13] showed that the Ar–NH_3 interaction splits the $j=1,|k|=1$ NH_3 state into one Σ and two Π levels. These levels are labeled Σ, Π_{upper}, and Π_{lower} in the figure. Here, we are using diatomic-molecule-like notation to designate the states. In this notation Σ and Π denote states with $|K|=0$ and 1, respectively, where K (called Ω in Refs. 13, 14) gives the projection of the total angular momentum J onto the pseudodiatomic axis of the complex. As discussed by Hutson for Ar–H_2O, for sufficiently high internal-rotation barriers K is nearly a good quantum number.

Approximate "zero-point" pictures of the Σ and two Π states are shown in Fig. 2. The present measurements do not allow us to determine which of the two Π geometries belong to the observed Π_{lower} and Π_{upper} states. The *ab initio* calculations of Bulski *et al.*,[12] though, indicate that the potential energy is lower for the configuration in which the H atoms are directed away from the Ar, so that the Π_{lower} configuration corresponds to the geometry shown in the bottom of Fig. 2.

In Ar–NH_3, NH_3 tunneling further splits the Σ and Π levels into a symmetric and an antisymmetric tunneling component, denoted by an "s" or "a" subscript on the Σ and Π labels. The origin of the tunneling effects can be appreciated by examination of Fig. 2. The presence of the Ar makes the NH_3 inversion potential extremely asymmetric for the Π states, but not so for the Σ state. Because of this, the NH_3 tunneling is effectively quenched in the Π states and almost unaffected in the Σ state. The small splittings of the Π states shown in Fig. 1 are Coriolis-induced tunneling splittings driven by interactions of the Π states with the nearby Σ states. If the Coriolis coupling is weak, the J dependence of

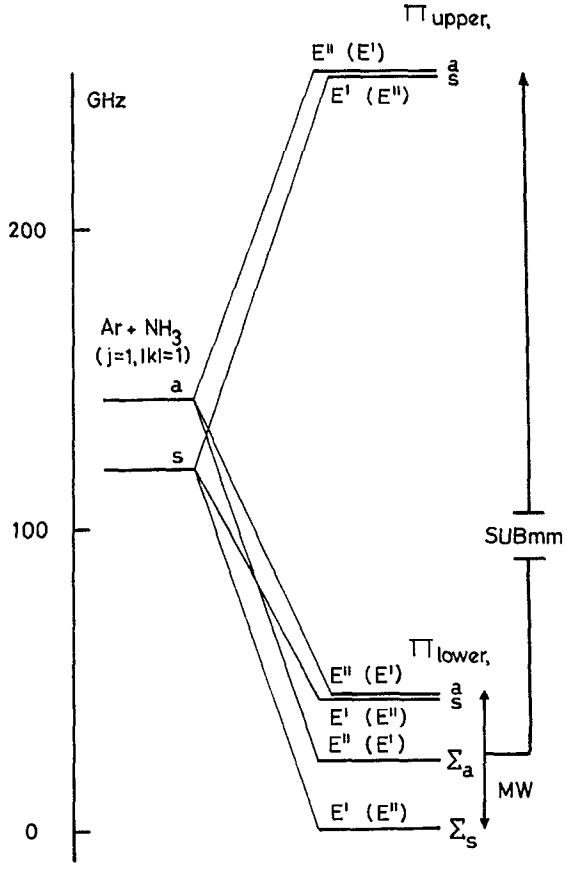

FIG. 1. Energy level scheme of Ar–NH_3 states correlating with Ar + NH_3 ($j = 1, |k| = 1$). The zeroes of energy for the Ar–NH_3 and Ar + NH_3 states are not the same, differing by approximately the zero-point binding energy of the complex. The rovibronic symmetries are given for even J, with the odd-J symmetries enclosed in parentheses. For the Π states the splitting between the Π_{lower} and Π_{upper} state is not due to tunneling, but instead is a measure of the energy difference of the two different "zero-point" geometries shown for the Π states in Fig. 2. The smaller E'–E'' splittings for the Π_{lower} and Π_{upper} states arise from the NH_3 inversion, as does the larger splitting between the Σ_s and Σ_a states.

the splittings resembles that typically seen for l doubling in a linear molecule or K doubling in an asymmetric top. In the text we will refer to this splitting as l doubling or tunneling doubling.

End-over-end rotation gives rise to a series of Σ levels with $J = 0,1,2,...$ and Π levels with $J = 1,2,3,...$ The symmetries of the rotation internal–rotation tunneling states under the molecular symmetry group D_{3h} (M)[24] are also given in Fig. 1. The symmetries are given for even J, with the odd J symmetries enclosed in parentheses. The Coriolis interaction between the Σ and Π states only mixes states of the same J and of the same symmetry under $D_{3h}(M)$. The observed microwave transitions are within and between the four lowest lying internal-rotor levels of Fig. 1. The submillimeter transitions are between the four lowest and the two highest lying levels. The electric-dipole selection rules are $E' \leftrightarrow E''$ with $\Delta J = 0, \pm 1$.

The observed microwave transition frequencies are listed in Table I. We also tabulate the hyperfine corrected microwave frequencies when hyperfine splittings are observed. These corrected frequencies have been used in the fit described below. The observed submillimeter transitions are given in Table II. The submillimeter transitions showed no hyperfine splittings at the FM amplitude which resulted in the largest signals. The frequencies measured with these optimum FM amplitudes have been used in the fit. Upon lowering of the FM amplitude half of the transitions showed resolved hyperfine structure, but still the resolution was insufficient to determine reliable quadrupole coupling constants.

Since the microwave spectrum is strongly perturbed by the Π–Σ Coriolis interaction, the initial assignments of the microwave transitions were made by using the observed hyperfine patterns to identify the J states of the transitions and by using microwave–microwave double-resonance experiments. The latter experiments were done by exploiting the double-resonance capabilities of the MBER and EROS spectrometers. The assignment of the first submillimeter lines, which were $\Pi \leftarrow \Sigma$ transitions, was easier since the spectrum consists of two bands, similar in structure to vibrational bands, both with P, Q, and R branches. The assigned microwave and submillimeter transitions turned out to involve

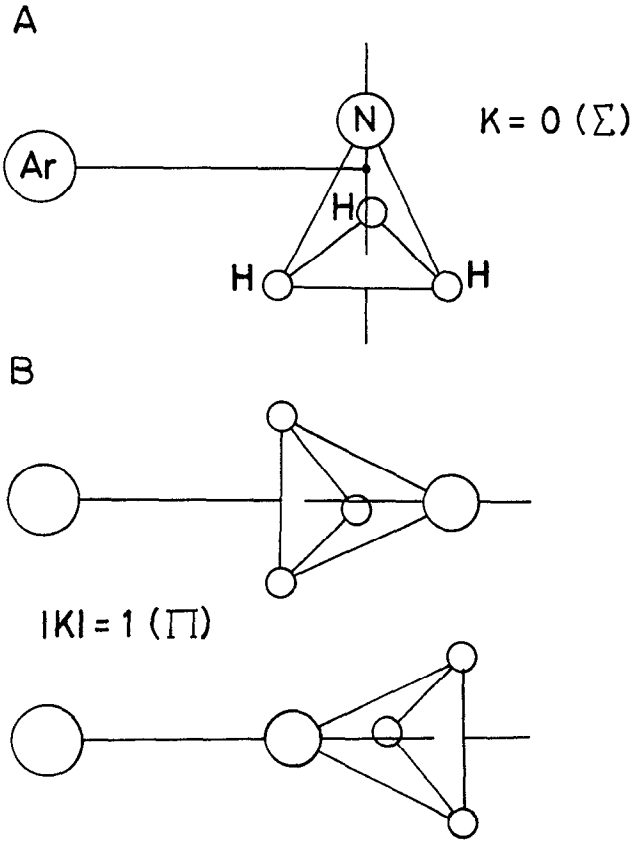

FIG. 2. Approximate "zero-point" geometries for the Σ and Π states from Fig. 1.

TABLE I. Observed microwave transitions (in MHz) for the Ar–NH_3 states correlating with Ar + NH_3 ($j = 1, |k| = 1$).[a]

	J'	J''	F'	F''	Sym′	Sym″	Frequency	Obs − Cal
$\Sigma_a - \Sigma_s$	1	1			E'	E''	22 283.191	0.113
	2	2			E''	E'	21 661.723	−0.055
	3	3			E'	E''	21 025.297	−0.119
	4	4			E''	E'	20 477.477	−0.058
	5	5			E'	E''	20 048.820	0.086
	6	6			E''	E'	19 734.921	0.098
			6	6			19 734.881	
			5	5			19 734.942	
			7	7			19 734.942	
	7	7			E'	E''	19 519.696	0.014
			7	7			19 519.656	
			6	6			19 519.717	
			8	8			19 519.717	
	8	8			E''	E'	19 385.152	−0.142
			7	7			19 385.172	
			9	9			19 385.172	
	9	9			E'	E''	19 315.249	0.052
			8	8			19 315.269	
			10	10			19 315.269	
	10	10			E''	E'	19 297(2)	1.874
$\Sigma_s - \Sigma_s$	3	2			E''	E'	15 326.304	−0.042
			4	3			15 326.303	
			3	2			15 326.303	
			2	1			15 326.371	
	4	3			E'	E''	20 628.994	−0.015
$\Sigma_a - \Sigma_a$	3	2			E'	E''	14 689.878	−0.107
			4	3			14 689.877	
			3	2			14 689.877	
			2	1			14 689.943	
	4	3			E''	E'	20 081.179	0.051
			5	4			20 081.187	
			4	3			20 081.187	
			3	2			20 081.187	
$\Pi_{lower} - \Sigma_s$	1	2			E''	E'	36 601.36	−0.226
	2	3			E'	E''	34 186.98	−0.234
	3	4			E''	E'	32 783.53	−0.189
	4	5			E'	E''	32 177.78	−0.049
	5	6			E''	E'	32 186.82	0.031
$\Pi_{lower} - \Sigma_a$	1	2			E'	E''	15 315.276	−0.046
			1	2			15 314.877	
			2	2			15 315.010	
			2	3			15 315.374	
			1	1			15 315.451	
			0	1			15 315.774	
	2	3			E''	E'	14 091.851	0.125
			2	3			14 091.505	
			3	3			14 091.619	
			3	4			14 091.966	
			1	2			14 092.155	
	3	4			E'	E''	13 771.678	0.090
			3	4			13 771.361	
			4	4			13 771.442	
			4	5			13 771.789	
			2	3			13 771.917	
	4	5			E''	E'	14 006.741	−0.080
			4	5			14 006.439	
			5	5			14 006.510	
			5	6			14 006.857	
			3	4			14 006.944	
	5	6			E'	E''	14 587.193	−0.176
			5	6			14 586.904	
			6	7			14 587.304	
			4	5			14 587.381	
	6	7			E''	E'	15 387.754	−0.036
			6	7			15 387.471	
			7	8			15 387.860	
			5	6			15 387.938	
	7	8			E'	E''	16 331.178	0.229
			7	8			16 330.896	
			8	9			16 331.290	
			6	7			16 331.354	
	8	9			E''	E'	17 367.465	−0.094
			8	9			17 367.182	
			9	10			17 367.576	
			7	8			17 367.642	
	1	1			E''	E'	24 448.31	−0.463
	2	2			E'	E''	27 851.59	−0.192
	3	3			E''	E'	32 387.27	−0.042
	4	4			E'	E''	37 724.83	−0.032
	1	0			E'	E''	29 448.97	−0.447
	2	1			E''	E'	38 290.45	−0.225
$\Pi_{lower} - \Pi_{lower}$	2	1			E''	E'	13 466.453	0.064
			1	0			13 466.323	
			2	2			13 466.323	
			3	2			13 466.461	
			2	1			13 466.461	
			1	1			13 466.662	
	2	1			E'	E''	12 911.937	−0.037
	3	2			E'	E''	19 761.006	0.016
			2	1			19 760.955	
			4	3			19 761.000	
			3	2			19 761.034	
	3	2			E''	E'	19 225.560	0.046

[a] Experimental uncertainties in the frequency measurements are approximately 5 in units of the last significant digit.

common levels. A collaborative effort resulted in many new assigned lines, e.g., the $\Sigma \leftarrow \Sigma$ microwave direct-inversion transitions and the weak $\Pi \leftarrow \Pi$ submillimeter bands.

The observed microwave and submillimeter transitions are consistent with Fig. 1 and the relative energies in the figure are drawn to scale. The two data sets are also consistent with each other, as verified by using combination differences. An assignment to the ortho Ar–NH_3 $\Sigma(j = 0, k = 0)$ ground state can be excluded since this state is well characterized and shows no common combination differences or effective rotational constants with the states presented here.

All assigned frequencies have been fit to effective rotational constants by using the following energy-level expression for each of the six levels drawn in Fig. 1,

$$E_{i,J} = E_i + B_i J(J+1) - D_i J^2 (J+1)^2, \qquad (1)$$

where E_i is the energy-level origin, and B_i and D_i are rotation and distortion constants of level i. Off-diagonal Coriolis matrix elements $\alpha_{\Sigma\Pi}\sqrt{J(J+1)/2}$ were used between the lowest Σ and Π states, i.e., between levels Σ_s and $\Pi_{lower,s}$ and between levels Σ_a and $\Pi_{lower,a}$. The Coriolis coupling of the Σ states to the upper Π states was not included in the analysis since the coupling of these states is sufficiently weak that the Π_{upper} levels are well characterized using a single B and D_J for the s component and a single B and D_J for the a component. In addition, due to larger energy separation of the Σ

TABLE II. Observed submillimeter transitions (in MHz) for the Ar–NH_3 states correlating with Ar + NH_3 ($j = 1, |k| = 1$).[a]

	J'	J''	Sym′	Sym″	Frequency	Obs − Cal
Π_{upper}–Σ_s	1	2	E''	E'	241 945.44	0.15
	2	3	E'	E''	238 036.13	0.16
	3	4	E''	E'	234 528.38	0.24
	4	5	E'	E''	231 323.90	0.19
	5	6	E''	E'	228 344.30	0.04
	6	7	E'	E''	225 530.80	−0.13
	7	8	E''	E'	222 840.88	−0.24
	8	9	E'	E''	220 244.81	−0.01
	9	10	E''	E'	217 722.20	0.80
	1	1	E'	E''	252 110.37	−0.06
	2	2	E''	E'	253 467.13	0.01
	3	3	E'	E''	255 367.41	0.03
	4	4	E''	E'	257 700.06	0.02
	5	5	E'	E''	260 366.09	0.03
	6	6	E''	E'	263 286.24	−0.08
	7	7	E'	E''	266 401.34	−0.10
	8	8	E''	E'	269 668.49	−0.07
	9	9	E'	E''	273 057.77	0.23
	10	10	E''	E'	276 548.97	1.08
	1	0	E''	E'	257 109.49	−0.04
	2	1	E'	E''	263 492.53	−0.05
	3	2	E''	E'	270 483.62	0.12
	4	3	E'	E''	277 977.45	0.16
	5	4	E''	E'	285 860.64	0.22
	6	5	E'	E''	294 031.38	0.07
	7	6	E''	E'	302 408.03	−0.02
	8	7	E'	E''	310 928.11	−0.21
	9	8	E''	E'	319 545.79	−0.26
	10	9	E'	E''	328 227.76	0.01
Π_{upper}–Σ_a	1	2	E'	E''	220 318.56	0.18
	2	3	E''	E'	217 115.53	0.17
	3	4	E'	E''	214 260.96	0.12
	4	5	E''	E'	211 626.66	−0.08
	5	6	E'	E''	209 139.42	−0.23
	6	7	E''	E'	206 757.63	−0.22
	7	8	E'	E''	204 457.94	−0.06
	8	9	E''	E'	202 228.06	0.06
	9	10	E'	E''	200 062.61	−0.51
	1	1	E''	E'	229 792.32	−0.16
	2	2	E'	E''	231 700.80	0.26
	3	3	E''	E'	234 132.05	0.31
	4	4	E'	E''	236 871.02	0.27
	5	5	E''	E'	239 787.22	0.10
	6	6	E'	E''	242 804.76	−0.13
	7	7	E''	E'	245 879.41	−0.17
	8	8	E'	E''	248 984.73	−0.15
	9	9	E''	E'	252 105.43	−0.07
	1	0	E'	E''	234 452.11	−0.37
	2	1	E''	E'	241 314.13	−0.18
	3	2	E'	E''	249 032.01	0.06
	4	3	E''	E'	257 303.79	0.16
	5	4	E'	E''	265 913.23	0.14
	6	5	E''	E'	274 729.17	0.00
	7	6	E'	E''	283 675.30	−0.11
	8	7	E''	E'	292 707.00	−0.02
	9	8	E'	E''	301 797.80	0.19
	10	9	E''	E'	310 932.13	0.15
	11	10	E'	E''	320 101.51	−0.86
Π_{upper}–Π_{lower}	3	4	E''	E'	176 325.88	0.13
	3	4	E'	E''	174 658.25	0.00
	2	2	E''	E'	203 953.84	0.28
	3	3	E'	E''	201 954.86	0.20
	4	4	E''	E'	199 497.66	0.02
	5	5	E'	E''	196 687.45	−0.23
	6	6	E''	E'	193 611.13	−0.43
	7	7	E'	E''	190 337.55	−0.32
	8	8	E''	E'	186 920.90	0.68
	1	1	E''	E'	204 968.30	0.11
	2	2	E'	E''	202 918.92	0.09
	3	3	E''	E'	200 279.13	0.11
	4	4	E'	E''	197 268.31	0.15
	5	5	E''	E'	194 022.16	0.09
	6	6	E'	E''	190 623.33	−0.13
	7	7	E''	E'	187 124.53	−0.34
	8	8	E'	E''	183 562.01	−0.05
	2	1	E'	E''	216 761.00	0.27
	3	2	E''	E'	220 970.27	0.33
	4	3	E'	E''	224 564.88	0.32
	5	4	E''	E'	227 658.20	0.17
	6	5	E'	E''	230 352.82	−0.11
	7	6	E''	E'	232 732.94	−0.36
	8	7	E'	E''	234 864.29	−0.45
	9	8	E''	E'	236 798.16	0.45
	2	1	E''	E'	216 490.23	0.21
	3	2	E'	E''	220 250.23	−0.01
	4	3	E''	E'	223 450.89	−0.03
	5	4	E'	E''	226 310.52	0.02
	6	5	E''	E'	228 964.13	0.01
	7	6	E'	E''	231 493.85	−0.12
	8	7	E''	E'	233 952.07	−0.24
	9	8	E'	E''	236 375.09	0.30

[a] Experimental uncertainties in the frequency measurements are approximately 0.10 MHz.

and Π_{upper} states it is possible that other unobserved Σ states contribute significantly to the Coriolis splittings in the Π_{upper} states. The E_i's are taken relative to the lowest energy $\Sigma_s(j = 1, |k| = 1)$ level by setting $E(\Sigma_s) = 0$. The energy-level origins of the two Coriolis-split Π_{lower} states were constrained to be equal. The same constraint was used for the two Π_{upper} levels. It was found that for the Coriolis-coupled states the best B and D constants to report are the sum and difference of the constants for the two coupled states. The difference is strongly correlated with the Coriolis constant, while the sum is not, and therefore the error in the sum is small relative to that of the difference. In Table III we list the constants obtained from the fit, with the residuals from the fit being given in Tables I and II. Note in the table that the Σ_a–Σ_s splitting of 22.7 GHz is nearly identical to the free NH_3 inversion splitting of 23.8 GHz, indicating that for the Σ states the NH_3 inversion splitting is only weakly affected by complexation.

The magnitude of the Coriolis-induced splittings (l-doubling) in the Π states can be taken as a direct measure of the NH_3 inversion splitting in these states since these splittings would be absent in the case of an Ar complex with a noninverting symmetric top, such as Ar–PH_3. The l-doublet splittings are significantly larger for the Π_{lower} state than for the Π_{upper} state due to the near degeneracy of the interacting Σ and Π_{lower} states. The combination-difference calculated splittings for the $J = 1$, 2 and 3 levels of the Π_{lower} states are 376, 930, and 1466 MHz, respectively, compared to the 35, 105, and 210 MHz splitting found for the Π_{upper} state. For

TABLE III. (a) Band origins obtained from the fit (in MHz). (b) Effective constants of the Σ_s,Σ_a, and Π_{lower} states obtained from the fit (in MHz). (c) Effective constants of the Π_{upper} states obtained from the fit (in MHz).

(a)		Σ_s	Σ_a	Π_{lower}	Π_{upper}
	E	0[a]	22 691.922(45)	45 276.381(71)	251 400.15(30)
(b)			Σ_s;$\Pi_{lower,s}$	Σ_a;$\Pi_{lower,a}$	
	$(B_\Sigma + B_\Pi)/2$		2881.0463(50)	2872.7229(42)	
	$(B_\Sigma - B_\Pi)/2$		−21.8(10)	−16.56(13)	
	$(D_\Sigma + D_\Pi)/2$		0.095 81(14)	0.100 47(11)	
	$(D_\Sigma - D_\Pi)/2$		−0.034 06(82)	−0.118 265(86)	
	$\alpha_{\Sigma\Pi}$		5613.4(81)	5080.20(62)	
(c)			$\Pi_{upper,s}$	$\Pi_{upper,a}$	
	B		2854.834(10)	2872.251(14)	
	D		0.072 41(14)	0.063 84(13)	

[a] Constrained in the fit.

the Π_{upper} state the splittings are in the 1:3:6 ratio expected for *l*-type (or *K*-type) doubling in a linear (or asymmetric top) molecule.

Using the procedure described in the experimental section, relative integrated absorption intensities have been determined for several submillimeter transitions. The results for the various transitions between levels of para Ar–NH_3 are discussed in a following section. There these results are compared with theoretical calculations. We have also compared the intensities of the submillimeter bands presented in the present paper, i.e., those of para Ar–NH_3 with two already known bands between levels of ortho Ar–NH_3. The intensities of four $R(3)$ transitions have been determined, one shortly after the other, using harmonics from a klystron operating around 70 GHz. Only the grating of the monochromator had to be changed between the different measurements. In this way equal conditions are obtained to ensure the reliability of the measurements. The results are listed in Table IV.

TABLE IV. Measured relative integrated absorption intensities[a] of several submillimeter $R(3)$ transitions.[b]

Transition	Form	Frequency	Intensity
$\Pi \leftarrow \Pi$, $R(3)$[c]	Para	224 564.88	2.0
$\Pi \leftarrow \Sigma$, $R(3)$[c]	Para	277 977.45	31
$\Pi \leftarrow \Sigma$, $R(3)$[d]	Ortho	513 607.96	1000
$\Sigma \leftarrow \Sigma$, $R(3)$[e]	Ortho	815 476.28	397

[a] The estimated uncertainties in the measured intensities are 30%.
[b] The frequencies are in MHz. Experimental uncertainties in the frequency measurements are 0.10 MHz.
[c] This work.
[d] References 7 and 8.
[e] Reference 6.

IV. DYNAMICAL MODEL

The rotation internal-rotation tunneling states of Ar–NH_3 can be modeled using an extension of the rod–ball and asymmetric-top-ball descriptions applied previously to the rare-gas hydrogen halide and Ar–H_2O complexes.[25] Here, we will consider an inverting and rotating NH_3 unit coupled to an Ar atom through an interaction potential V. We will constrain all the coordinates of the NH_3 unit at their "zero-point" values, except for the tunneling coordinate α. Also, since we are mainly interested in characterizing the internal-rotation inversion states of the complex and since we do not study states with excitation of the radial coordinate, we will further reduce the dimensionality of the problem by fixing the radial coordinate R at an effective center of mass separation R_{cm}. With these considerations, the Hamiltonian for the Ar–NH_3 complex can be expressed as

$$H = H_{rot} + h_{inv}(\alpha) + V(\theta,\phi,\alpha), \tag{2}$$

where

$$H_{rot} = B_d \mathbf{l}^2 + b(\alpha)\mathbf{j}^2 + [c(\alpha) - b(\alpha)]\mathbf{j}_c^2, \tag{3}$$

$B_d = \hbar^2/(2\mu R_{cm}^2)$, μ is the pseudo-diatomic reduced mass, $\mathbf{l}$ is the orbital angular momentum associated with end-over-end rotation of the complex, $\mathbf{j}$ is the angular momentum of the NH_3 unit with projection $\mathbf{j}_c$ along the NH_3 symmetry axis (i.e., c axis), $b(\alpha)$ and $c(\alpha)$ are the rotational constants of NH_3 as a function of α, h_{inv} is the inversion Hamiltonian for free NH_3, and $V(\theta,\phi,\alpha)$ is the interaction potential between Ar and NH_3. The polar coordinates (R,θ,ϕ) specify the orientation of the Ar with respect to an (x,y,z) Cartesian axis system fixed on the NH_3 with origin at the NH_3 center of mass and z axis along the NH_3 symmetry axis, as shown in Fig. 3. Although for our purposes the definition of the tunneling coordinate is somewhat arbitrary, for convenience we will take α to be the angle between the N–H bonds and the negative z axis.

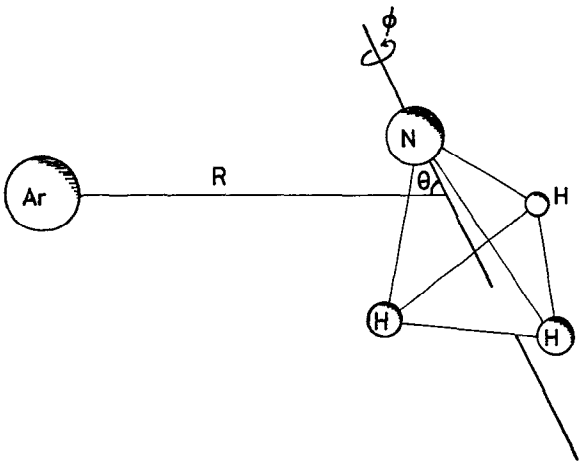

FIG. 3. The polar coordinates (R,θ,ϕ) specifying the position of the Ar atom relative to the NH_3 frame.

Matrix elements of H are evaluated in the coupled basis, $|JMjklv\rangle$, where $\mathbf{J}=\mathbf{l}+\mathbf{j}$, constructed from products of spherical harmonics $Y_{l,m_l}(\theta_{sf},\phi_{sf})$, symmetric-top functions $D^{j*}_{m,k}(\alpha_1,\beta_1,\gamma_1)$,[26] and NH_3 tunneling wave functions $\Psi_v(\alpha)(v=0,1,...)$. Here, θ_{sf} and ϕ_{sf} are the polar coordinates necessary to specify the orientation of a unit vector along R with respect to some space-fixed (X,Y,Z) axis system, and $(\alpha_1,\beta_1,\gamma_1)$ are the Euler angles between the NH_3 body-fixed axis system and this same space-fixed axis system. To simplify the evaluation of matrix elements of $V(\theta,\phi,\alpha)$, we expand $V(\theta,\phi,\alpha)$ in renormalized spherical harmonics,[26] $C_{pq}(\theta,\phi)$ as

$$V(\theta,\phi,\alpha)=\sum_{-p<q<p\wedge p>0} v_{pq}(\alpha)C_{pq}(\theta,\phi), \tag{4}$$

where the v_{pq} are independent of θ and ϕ. Consideration of the transformation properties of θ, ϕ and α in the molecular symmetry group of Ar–NH_3, which is identical to that used to characterize free NH_3 and is denoted $D_{3h}(M)$,[24] allows us to reexpress Eq. (4) as

$$V(\theta,\phi,\alpha)=\frac{1}{6}\sum_{-p<q<p\wedge p>0}\left[1+2\cos\left(\frac{2\pi q}{3}\right)\right]V_{pq}(\alpha) \times[C_{pq}(\theta,\phi)+(-1)^q C_{p-q}(\theta,\phi)], \tag{5}$$

where

$$V_{pq}(\alpha)=\tfrac{1}{2}[(-1)^{p-q}v_{pq}(\pi-\alpha)+v_{pq}(\alpha)]. \tag{6}$$

The matrix element of $H_{\rm rot}+h_{\rm inv}$ are diagonal in the $|JMjklv\rangle$ basis,

$$\langle JMjklv|H|JMjklv\rangle = B_a l(l+1)+b_\omega j(j+1) + (c_v-b_v)k^2+w_v, \tag{7}$$

where the w_v's are the term values of the NH_3 inversion potential, with $w_1-w_0=0.793\,408\,3\ \text{cm}^{-1}$ being the NH_3 ground-state tunneling splitting. Also in Eq. (7), $b_0=9.946\,642\,2\ \text{cm}^{-1}$, $b_1=9.941\,588\,7\ \text{cm}^{-1}$, $c_0-b_0=-3.719\,920\,4\ \text{cm}^{-1}$, and $c_1-b_1=-3.712\,867\,6\ \text{cm}^{-1}$, are the zero-point rotational constants for the symmetric and antisymmetric tunneling states of free NH_3, as determined by Urban *et al.*[1] The potential matrix elements are both diagonal and off-diagonal in j, k, l, and v.

$$\langle JMj'k'l'v'|V(\theta,\phi,\alpha)|JMjklv\rangle = \frac{1}{6}\sum_{-p<q<p\wedge p>0}\left[1+2\cos\left(\frac{2\pi q}{3}\right)\right]\langle v'|V_{pq}(\alpha)|v\rangle(-1)^{J-k+l'+l}[(2l'+1)(2l+1)(2j'+1)(2j+1)]^{1/2} \times\begin{pmatrix} l & p & l' \\ 0 & 0 & 0\end{pmatrix}\left[\begin{pmatrix} j' & p & j \\ k' & q & -k\end{pmatrix}+(-1)^q\begin{pmatrix} j' & p & j \\ k' & -q & -k\end{pmatrix}\right]\begin{Bmatrix} l' & j' & J \\ j & l & p\end{Bmatrix}. \tag{8}$$

Note that these matrix elements vanish for $q\neq 0,3,6,...$ and that for $(p-q)$ even, $(v'-v)$ must be even, while for $(p-q)$ odd, $(v'-v)$ must be odd.

The Hamiltonian matrix which results can be symmetry factored into A_1', A_1'', A_2', A_2'', E' and E'' blocks in $D_{3h}(M)$, with the E' and E'' blocks being of interest here since only these rovibronic species can result from $Ar+NH_3$ $(j=1,|k|=1)$. For the E' and E'' states, the symmetry adapted wave functions take the following form,

$$\begin{aligned} E'&\begin{cases}|JMjklv\rangle & l+v \text{ odd}, \quad k=6n\pm 1\\ |JMjklv\rangle & l+v \text{ even} \quad k=6n\pm 2\end{cases}\\ E''&\begin{cases}|JMjklv\rangle & l+v \text{ odd} \quad k=6n\pm 2\\ |JMjklv\rangle & l+v \text{ even}, \quad k=6n\pm 1\end{cases}\end{aligned} \tag{9}$$

where $n=0,\pm 1,\pm 2,...$.

The Hamiltonian matrix H was set up in the $|JMjklv\rangle$ basis set including interactions from $j=1...8$, $k=\pm 1$, and $v=0,1$, and diagonalized to determine energies. States with $v>1$ correspond to excited vibrational states of NH_3, and were not included here since the v_2 vibrational frequency of approximately 950 cm^{-1} is expected to be substantially greater than the $\langle v=2,3|V_{pq}|v'=0,1\rangle$ matrix elements coupling the ground state to the excited state. Values for $\langle v|V_{pq}|v'\rangle$ were determined iteratively from fitting the experimental data to the energies obtained from the diagonalization of H, as discussed later. Terms up to $\langle v'|V_{20}|v\rangle$ in Eq. (8) were considered. We have not considered higher-order terms since these are expected to be much smaller and the present experimental data are not sufficient to examine these in detail. This allows us to limit our basis set to states with $|k|=1$.

The electric-dipole selection rules are $E'\leftrightarrow E''$. The dipole moment matrix elements necessary to calculate transition intensities are obtained from

$$\langle J'M'j'k'l'v'|\mu_Z|JMjklv\rangle = \delta_{MM'}\delta_{ll'}\mu_{vv'}(-1)^{j+J'-k}[(2J+1)(2J'+1)(2j+1)(2j'+1)]^{1/2}\begin{pmatrix} j & 1 & j' \\ -k & 0 & k' \end{pmatrix} \times \sum_{m=-j}^{j}(-1)^m\begin{pmatrix} j & l & J \\ m & M-m & -M \end{pmatrix}\begin{pmatrix} j' & l & J' \\ m & M-m & -M \end{pmatrix}\begin{pmatrix} j & 1 & j' \\ -m & 0 & m \end{pmatrix}, \quad (10)$$

where $\mu_Z = \mu(\alpha)\cos(\beta_1)$ is the projection of the NH_3 dipole moment onto the space-fixed Z axis along which M is quantized. We define $\mu_{vv'} \equiv \langle v|\mu(\alpha)|v'\rangle$, where $\mu_{01} = 1.47$ D is the ground state dipole moment of free NH_3. Note that $\mu_{vv'} = 0$ for $(v - v')$ even.

Following Fraser *et al.* for Ar–H_2O,[27] effective quadrupole coupling constants, eqQ_{eff}, are calculated for each rotation internal-rotation tunneling state via first-order perturbation theory using the zeroth-order diagonal in J matrix elements of the electric quadrupole interaction,

$$\langle FM_FJj'k'l'v'|H_Q|FM_FJjklv\rangle = \langle v'|eqQ_{cc}(\alpha)|v\rangle\delta_{ll'}(-1)^{J+l'+j'+j-k}[(2j'+1)(2j+1)]^{1/2}f(I,J,F) \times\left(\frac{(2J-1)(2J+1)(2J+3)}{J(J+1)}\right)^{1/2}\begin{Bmatrix} J & J & 2 \\ j & j' & l' \end{Bmatrix}\begin{pmatrix} j' & 2 & j \\ k' & 0 & -k \end{pmatrix} \quad (11)$$

and the eigenvectors from the diagonalization of H. Here, $\mathbf{F} = \mathbf{I} + \mathbf{J}$, where $I = 1$ is the ^{14}N nuclear spin, $f(I,J,F)$ is, as before, Casimir's function, and $eqQ_{cc}(\alpha)$ is the c-axis (i.e., symmetry axis) component of the quadrupole coupling tensor of free NH_3 as a function of the tunneling coordinate. Note that $\langle v'|eqQ_{cc}(\alpha)|v\rangle = 0$ for $(v' - v)$ odd and $\langle 1|eqQ_{cc}(\alpha)|1\rangle \approx \langle 0|eqQ_{cc}(\alpha)|0\rangle \equiv eqQ^{NH_3}$ the quadrupole coupling constant of free NH_3. We use $eqQ^{NH_3} = -4.089\,83$ MHz, as determined by Marshall and Muenter.[28]

V. DETERMINATION OF THE POTENTIAL ENERGY SURFACE

As discussed in the previous section, the Hamiltonian is diagonalized using potential parameters V_{00}, V_{10}, and V_{20}. For B_d in Eqs. (3) and (7) the mean value of the six B_i's has been used. This average $B = 2872.4$ MHz has no first-order Coriolis or angular-radial coupling effects, and is close to the B value of 2876.8 MHz found by Nelson *et al.*[5] for the $\Sigma(j = 0, k = 0)$ state of Ar–NH_3. As an aside, we note that the mean D value of 0.0881 MHz determined here is also nearly identical to that found for the $\Sigma(j = 0, k = 0)$ state where $D = 0.0887$ MHz. With the B_d constraint above, the energy level positions E_i of Table IIIa are only functions of the potential matrix elements $\langle v'|V_{pq}|v\rangle$, and these matrix elements can consequently be iteratively determined. The maximum number of independent matrix elements, corresponding to the number of available band origins, is three. The potential matrix elements are not constrained by symmetry to be identical for the two tunneling states. Since we do not have sufficient data to determine all the V_{i0}, one of the constraints, $\langle 0|V_{00}|0\rangle = \langle 1|V_{00}|1\rangle$ or $\langle 0|V_{20}|0\rangle = \langle 1|V_{20}|1\rangle$, has been used in the calculations. The potential matrix elements were then determined by fitting the experimental $J = 0$ Σ levels and the $J = 1$ Π levels to the V_{i0}. For the $J = 1$ Π levels the average of the two l-doublet split levels were fit. The potential matrix elements determined from the model are listed in Table V.

The potential matrix elements from Table V can be used to calculate transition intensities and quadrupole coupling constants to compare with experiment. This will further test the model used and the validity of truncating the potential expansion at V_{20}, which is equivalent to assuming free internal rotation of the NH_3 about its symmetry axis.

The quadrupole coupling constants for some of the lower J states are known from the microwave measurements. As in Ref. 27, for every J level an effective quadrupole constant eqQ_{eff} can be defined by

$$E_Q = eqQ_{\text{eff}}f(I,J,F), \quad (12)$$

TABLE V. Ar–NH_3 potential parameters (in cm^{-1}).

	Case 1 $\langle 0\|V_{20}\|0\rangle = \langle 1\|V_{20}\|1\rangle$	Case 2 $\langle 0\|V_{00}\|0\rangle = \langle 1\|V_{00}\|1\rangle$
$(\langle 1\|V_{00}\|1\rangle - \langle 0\|V_{00}\|0\rangle)/2$	−0.0111	0[a]
$\lvert\langle 0\|V_{10}\|1\rangle\rvert$	9.6709	9.6682
$(\langle 1\|V_{20}\|1\rangle - \langle 0\|V_{20}\|0\rangle)/2$	0[a]	0.0469
$(\langle 1\|V_{20}\|1\rangle + \langle 0\|V_{20}\|0\rangle)/2$	20.3797	20.3797
B_d	2872.4 MHz[a]	2872.4 MHz[a]

[a] Constrained in the fit.

where eqQ_{eff} is the coefficient of $f(I,J,F)$ in Eq. (11). The eqQ_{eff} are calculated from Eq. (12) using the wave functions obtained from the diagonalization of the Hamiltonian with the potential matrix elements from Table V. The results, which are given in Table VI, show good agreement with experiment. The eqQ_{eff} also do not differ appreciably for the two sets of potential parameters of Table V.

The wave functions obtained by diagonalization of H, together with the dipole moment matrix elements of Eq. (10), can be used to estimate intensities for the submillimeter bands. Figure 4 shows the calculated spectra for the $\Pi_{upper} \leftarrow \Sigma_s$, $\Pi_{upper} \leftarrow \Sigma_a$ and $\Pi_{upper} \leftarrow \Pi_{lower}$ bands. The simulations were done using a rotational temperature of 5 K, which approximately reproduces the observed intensity profiles. As seen in the figure, the $\Pi_{upper} \leftarrow \Sigma_s$ band is calculated to be 9 times stronger than the $\Pi_{upper} \leftarrow \Pi_{lower}$ band, as obtained by comparing the ratios of the strongest lines from the two bands. Experimentally we find an intensity ratio of approximately 10, in good agreement with the calculations.

The intensities also show a number of interesting anomalies resulting from the Σ–Π Coriolis interactions. The most striking of these is that experimentally the $\Pi \leftarrow \Pi$ submillimeter bands possess Q branches with intensity profiles which resemble those expected for a perpendicular band, whereas a parallel $|K| = 1 \leftarrow 1$ type branch structure might be expected. The theoretical calculations however agree with the experimental results and, in fact, show that most of the intensity for the $\Pi \leftarrow \Pi$ band comes from the Σ–Π Coriolos interaction, giving substantial $\Pi \leftarrow \Sigma$ or $|K| = 1 \leftarrow 0$ character to the $\Pi \leftarrow \Pi$ band.

In addition to the dramatic intensity features in the $\Pi \leftarrow \Pi$ band, the Σ–Π Coriolis interaction also gives rise to a strong $\Sigma \leftarrow \Sigma$ type Q branch in the microwave spectrum. In the absence of Coriolis interactions, the $\Sigma \leftarrow \Sigma$ Q branch is forbidden, since it would correspond to a pure $K = 0 \leftarrow 0$ (or $l = 0 \leftarrow 0$) Q branch for a symmetric top (linear molecule) for which the Hönl–London factors vanish. Here, the Coriolis interactions change a forbidden $K = 0 \leftarrow 0$ band into an allowed $|K| = 1 \leftarrow 0$ or $0 \leftarrow 1$ band through the rotationally induced admixture of $|K| = 1$ character into the $K = 0$ states.

Another interesting effect which is reproduced by the calculations is that experimentally several of the P branches

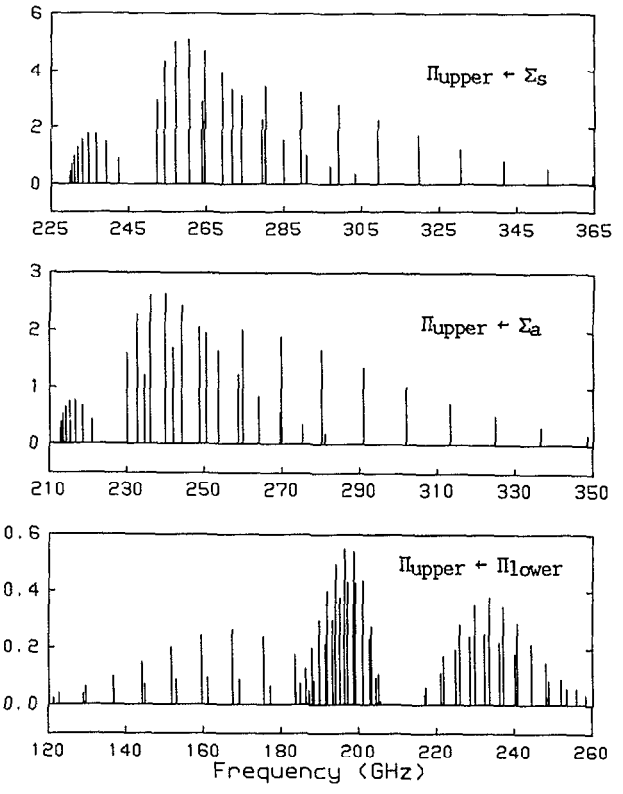

FIG. 4. Calculated spectrum for the observed submillimeter bands for $J = 0,12$. The calculations use the potential constants from Case 1 in Table V, a maximum j of 6 in the angular basis set and a rotational temperature of 5 K. The arbitrary intensity scale is the same for the three bands.

are found to be weaker than their R branch partners. For the $\Pi \leftarrow \Sigma$ bands this type of effect is expected from consideration of the Hönl–London factors for a $|K| = 1 \leftarrow 0$ type band. Here, we see for the $\Pi \leftarrow \Sigma$ bands that the difference in intensity between P and R branches is 2–3 in the experiments and 1.9–2.6 in the calculations (see Fig. 4). We have estimated the strength of a branch by the intensity of the strongest lines from the branch. For $\Pi \leftarrow \Pi$ bands this effect is also observed. For transitions between $\Pi_{lower,s}$ and $\Pi_{upper,s}$ the R

TABLE VI. Comparison of observed and calculated effective quadrupole coupling constants, eqQ_{eff}, (in MHz) for Ar–NH_3 states correlating with Ar + NH_3 ($j = 1, |k| = 1$). Calculations were done using the potential parameters of Case 1 in Table V and a maximum j of 7 in the free-rotor basis set.

State	$J = 1$	2	3	4	5
Σ_s	−1.1328	−1.1166	−1.0987	−1.0824	−1.0694
Σ_a	−1.2100	−1.1248	−1.0539	−1.0038	−0.9713
Observed		[−1.114(18)]	[−1.037(20)]	[−1.044(24)]	[−0.9999(43)]
$\Pi_{lower,s}$	−0.0148	−0.0287	−0.0398	−0.0465	−0.0472
$\Pi_{lower,a}$	0.4352	0.3523	0.2882	0.2477	0.2273
Observed	[0.444(12)]	[0.388(17)]	[0.250(26)]	[0.2076(50)]	
$\Pi_{upper,s}$	0.4476	−0.0625	−0.1962	−0.2564	−0.2938
$\Pi_{upper,a}$	0.0800	−0.4301	−0.5638	−0.6240	−0.6613

branch is calculated to be approximately five times stronger than the P branch. For transitions between $\Pi_{\text{lower,a}}$ and $\Pi_{\text{upper,a}}$ there are no large differences and the intensities are comparable. In both cases experiment and theory are in good agreement.

VI. DISCUSSION

The present results on the potential energy surface of Ar–NH_3 can be compared with recent dynamical calculations by van Bladel *et al.*[13,14] on an *ab initio* surface.[12] They found that by scaling the V_{33}-type term in the *ab initio* potential they obtained energy levels and intensities in reasonable agreement with the present measurements on the para Ar–NH_3 states and with previous measurements on the ortho Ar–NH_3 states. It must be noted that in the calculations of Refs. 13 and 14 the radial coordinate R is included. In our calculations an effective center of mass separation R_{cm} is used. The most striking difference between their calculations and our results is that van Bladel *et al.* find that V_{10} and $V_{33} = -V_{3-3}$ are the most important terms in the interaction potential, whereas we have used V_{10} and V_{20} and have assumed that V_{33} is negligible. The observation that the data can be fitted to a small V_{20} term is not too surprising since the θ dependencies of the V_{20} and V_{33} terms are quite similar. The main difference between the two terms is that V_{33} is also dependent on ϕ, the angle associated with the rotation of the NH_3 unit around its symmetry axis.

To test the sensitivity of our data to V_{33} we have fitted the experimental energy levels to V_{10} and V_{33} and find $|\langle 0|V_{10}|1\rangle| = 11.9803$ cm^{-1}, $\langle 0|V_{33}|0\rangle = -\langle 0|V_{3-3}|0\rangle = -46.8449$ cm^{-1} (or 46.8449 cm^{-1}), and $\langle 1|V_{33}|1\rangle = -\langle 1|V_{3-3}|1\rangle = -46.8855$ cm^{-1} (or 46.8855 cm^{-1}). We could have probably equally well fitted our data to $|\langle 0|V_{10}|1\rangle|$, $\langle 0|V_{ij}|0\rangle = (-1)^j\langle 0|V_{ij}|0\rangle$ and $\langle 1|V_{ij}|1\rangle = (-1)^j\langle 1|V_{ij}|1\rangle$, where $i+j$ is even. With increasing $i+j$, though, the potential constants must become increasingly large to obtain the observed energy level pattern. In fact, the V_{33}-type terms are already quite appreciable. For instance, at the T-shaped $\theta = 90°$ minimum-energy configuration, the fitted V_{33} terms imply a barrier of $\sqrt{5}|\langle i|V_{33}|i\rangle| \approx 100$ cm^{-1} for threefold rotation of the NH_3 unit about its symmetry axis. This barrier term is extremely large and not easily reconcilable with the <20 cm^{-1} barrier found for the "T-shaped" Ar–CH_3Cl.[29] For comparison, for the V_{00}, V_{10}, V_{20} fits of Table V the threefold barrier term is assumed to be zero everywhere.

The spectroscopic consequence of the large V_{33} term in Ar–NH_3 is to reduce the Coriolis interaction between the Π and Σ states by partially quenching the angular momentum arising from the internal rotation of the NH_3 unit about its symmetry axis. For instance, for the V_{10}, V_{20} fit we find a predicted l-type doubling splitting of 413 MHz for the $J = 1$ Π_{lower} state, compared to the observed value of 376 MHz. These can be compared to the V_{10}, V_{33} fit where we calculate an l-type doubling splitting of only 213 MHz. Future measurements on other internal-rotor states of the complex, as well as a direct fit of a potential to the rotation internal-rotation states of the complex, should allow us to probe more fully the balance between the V_{20} and V_{33} terms in the interaction potential.

VII. CONCLUSION

In the present work we have presented a detailed investigation of the spectroscopy and dynamics of the $j = 1, |k| = 1$ states of Ar–NH_3. The investigation of this species has permitted the examination of a well-studied problem,[30] the coupling of a two-level tunneling system to a larger system consisting of many degrees of freedom. The utility of such a study at high spectral resolution is dependent upon the ability to assign spectral lines and fit them to a Hamiltonian. As opposed to tunneling coupled to many degrees of freedom, in the present system a rich variety of behavior is found with only a few degrees of freedom. We have shown that the tunneling dynamics are strongly dependent upon the orientation of the tunneling NH_3 with respect to the radial coordinate. The Σ states with tunneling motion perpendicular to the radial coordinate show virtually unchanged behavior from free NH_3. The Π states with tunneling motion parallel to the radial coordinate have the tunneling motion nearly quenched. Coriolis interactions between the Π and Σ states lead to a rich and complicated spectrum. The present system now analyzed should serve as a convenient model for the investigation of the coupling of a tunneling mode to other degrees of freedom.

ACKNOWLEDGMENTS

The authors from Nijmegen wish to thank Professor J. Reuss for many stimulating discussions and Dr. M. Havenith, Professor A. van der Avoird, J. van Bladel, and Dr. P. Wormer for their interest in the experiments and for making their results available prior to publication. We would like to thank T. A. Fisher for assistance with the MBER measurements. G.T.F. would also like to thank C.A. Schmuttenmaer and R. C. Cohen for sending him a copy of their $k = 0$ work before publication and for several interesting discussions.

[1] S. Urban, D. Papousek, J. Kauppinen, K. Yamada, and G. Winnewisser, J. Mol. Spectrosc. **101**, 1 (1983).
[2] D. D. Nelson, Jr., G. T. Fraser, and W. Klemperer, Science **238**, 1670 (1987).
[3] G. T. Fraser, D. D. Nelson, Jr., A. Charo, and W. Klemperer, J.Chem. Phys. **82**, 2535 (1985).
[4] A. Bizzarri, B. Heijmen, S. Stolte, and J. Reuss, Z. Phys. D **10**, 291 (1988).
[5] D. D. Nelson, Jr., G. T. Fraser, K. I. Peterson, K. Zhao, W. Klemperer, F. J. Lovas, and R. D. Suenram, J. Chem. Phys. **85**, 5512 (1986).
[6] D. H. Gwo, M. Havenith, K. L. Busarow, R. C. Cohen, C. A. Schmuttenmaer, and R. J. Saykally, Mol. Phys. **71**, 453 (1990).
[7] C. A. Schmuttenmaer, R. C. Cohen, and R. J. Saykally, 45th Ohio State Symposium on Molecular Spectroscopy, Columbus, Ohio, June 1990.
[8] E. Zwart and W. L. Meerts, Chem. Phys. **151**, 407 (1991).
[9] B. J. Howard, Symposium on "Atomic and Molecular Clusters: Spectroscopy, Structures, and Dynamics," ACS National Meeting; Miami, Florida, September, 1989.
[10] G. T. Fraser, A. S. Pine, and W. A. Kreiner, J. Chem. Phys. **94**, 7061 (1991).
[11] G. Chałasiński, S. M. Cybulski, M. M. Szczęśniak, and S. Scheiner, J. Chem. Phys. **91**, 7809 (1989).

[12] M. Bulski, P. E. S. Wormer, and A. van der Avoird, J. Chem. Phys. **94**, 491 (1991).
[13] J. W. I. van Bladel, A. van der Avoird, and P. E. S. Wormer, J. Chem. Phys. **94**, 50 (1991).
[14] J. W. I. van Bladel, A. van der Avoird, and P. E. S. Wormer, J. Phys. Chem. (in press).
[15] F. J. Lovas and R. D. Suenram, J. Chem. Phys. **87**, 2010 (1987).
[16] R. D. Suenram, F. J. Lovas, G. T. Fraser, J. Z. Gillies, C. W. Gillies, and M. Onda, J. Mol. Spectrosc. **137**, 127 (1989).
[17] G. T. Fraser, R. D. Suenram, and L. H. Coudert, J. Chem.. Phys. **90**, 6077 (1989).
[18] G. T. Fraser, R. D. Suenram, L. H. Coudert, and R. S. Frye, J. Mol. Spectrosc. **137**, 244 (1989).
[19] E. Zwart, J. J. ter Meulen, and W. L. Meerts, Chem. Phys. Lett. **166**, 500 (1990).
[20] K. L. Busarow, G. A. Blake, K. B. Laughlin, R. C. Cohen, Y. T. Lee, and R. J. Saykally, J. Chem. Phys. **89**, 1268 (1988).
[21] J. M. Hutson, J. Chem. Phys. **92**, 157 (1990).
[22] R. C. Cohen, K. L. Busarow, K. B. Laughlin, G. A. Blake, M. Havenith, Y. T. Lee, and R. J. Saykally, J. Chem. Phys. **89**, 4494 (1988).
[23] R. C. Cohen, K. L. Busarow, Y. T. Lee, and R. J. Saykally, J. Chem. Phys. **92**, 169 (1990).
[24] P.R. Bunker, *Molecular Symmetry and Spectroscopy* (Academic, New York, 1979).
[25] See, for example, J. M. Hutson, in *Dynamics of Van Der Waals Complexes: Beyond Atom–Diatom Systems*, edited by N. Halberstadt and K. C. Janda (Plenum, New York, 1990).
[26] D. M. Brink and G. R. Satchler, *Angular Momentum* (Clarendon, Oxford, 1968).
[27] G. T. Fraser, F. J. Lovas, R. D. Suenram, and K. Matsumura, J. Mol. Spectrosc. **143**, 97 (1990).
[28] M. D. Marshall and J. S. Muenter, J. Mol. Spectrosc. **85**, 322 (1981).
[29] G. T. Fraser, R. D. Suenram, and F. J. Lovas, J. Chem. Phys. **86**, 3107 (1987).
[30] See, for instance: N. Makri and W. H. Miller, J. Chem. Phys. **86**, 1451 (1987); P. E. Parris and R. Silbey *ibid.* **86**, 6381 (1987).